# Electro- and Photocatalytic Conversion of $N_2$ to $NH_3$ by Chemically Modified Transition Metal Dichalcogenides, $MoS_2$, and $WS_2$

*Journal of The Electrochemical Society*, 2023 **170** 056501
1945-7111/2023/170(5)/056501/8/$40.00 © 2023 The Electrochemical Society ("ECS"). Published on behalf of ECS by IOP Publishing Limited

# Electro- and Photocatalytic Conversion of $N_2$ to $NH_3$ by Chemically Modified Transition Metal Dichalcogenides, $MoS_2$, and $WS_2$

**Ashwin Ganesan, Samar Alhowity, Ajyal Z. Alsaleh, Manan Guragain, Olatomide Omolere, Thomas R. Cundari,[z] Jeffry Kelber,[z] and Francis D'Souza[z,*]**

*Department of Chemistry, University of North Texas, 1155 Union Circle, #305070, Denton, TX 76203-5017, United States of America*

Electro- and photocatalytic reduction of $N_2$ to $NH_3$—the nitrogen reduction reaction (NRR)—is an environmentally- and energy-friendly alternative to the Haber-Bosch process for ammonia production. There is a great demand for the development of novel semiconductor-based electrocatalysts with high efficiency and stability for the direct conversion of inert substrates—including $N_2$ to ammonia—using visible light irradiation under ambient conditions. Herein we report electro-, and photocatalytic NRR with transition metal dichalcogenides (TMDCs), *viz* $MoS_2$ and $WS_2$. Improved acid treatment of bulk TMDCs yields exfoliated TMDCs (exTMDCs) only a few layers thick with ~10% S vacancies. Linear scan voltammograms on ex$MoS_2$ and ex$WS_2$ electrodes reveal significant NRR activity for exTMDC-modified electrodes, which is greatly enhanced by visible light illumination. Spectral measurements confirm ammonia as the main reaction product of electrocatalytic and photocatalytic NRR, and the absence of hydrazine byproduct. Femtosecond-resolved transient absorption studies provide direct evidence of interaction between photo-generated excitons/trions with $N_2$ adsorbed at S vacancies. DFT calculations corroborate $N_2$ binding to ex$MoS_2$ at S-vacancies, with substantial $\pi$-backbonding to activate dinitrogen. Our findings suggest that chemically functionalized exTMDC materials could fulfill the need for highly-desired, inexpensive catalysts for the sustainable production of $NH_3$ using Sunlight under neutral pH conditions without appreciable competing production of $H_2$.
 [DOI: 10.1149/1945-7111/acd02d]

Manuscript submitted November 11, 2022; revised manuscript received April 11, 2023. Published May 4, 2023.

Supplementary material for this article is available online

An important step towards achieving a sustainable society is the catalytic conversion of molecular nitrogen to ammonia under ambient conditions using renewable energy sources.[1–8] Ammonia, the key feedstock in the manufacturing of fertilizers needed in agriculture, is–due to its high-hydrogen content–potentially also important for the production of hydrogen fuel.[3] Thus, demand for $NH_3$ has increased steadily over the past 120 years. Global production reached 235 million metric tons in 2019 and is expected to reach 290 million metric tons by 2030. The current industrial production of $NH_3$ through the high temperature/pressure (300–500 °C, 20−30 MPa) Haber-Bosch process accounts for ~2% of global energy consumption while emitting large amounts of greenhouse gases, including $CO_2$.[9–12] Energy- and environmentally-friendly, economically-feasible routes to $NH_3$ production are urgently needed. In this regard, electrocatalytic, photocatalytic, and biological $N_2$ fixation strategies are being investigated by scientists all around the world.[1–6,13–17] Unfortunately, dinitrogen ($N_2$), the most commonly-used nitrogen feedstock in $NH_3$ manufacturing, is chemically and biologically inert due to its extremely strong, nonpolar triple bond (bond energy = 225 kcal $mol^{-1}$). Additionally, the weak binding strength of $N_2$ to most heterogeneous catalytic sites, the requirement of multi-electron and multi-proton processes in $N_2$ to $NH_3$ conversion, and competing reactions—including generation of hydrogen, hydrazine, and other byproducts—all suppress ammonia yields.[18–21]

For photocatalytic $NH_3$ production, various semiconductor photocatalysts, including $TiO_2$, $WO_3$, $Sm_2O_3/V_2O_3$, g-$C_3N_4$, $SrTiO_3$, and CdS, are known to convert $N_2$ to $NH_3$ under UV and/or visible light irradiation, often in the presence of organic scavengers or precious-metal cocatalysts. Importantly, in these traditional photocatalyst systems, the activation of $N_2$ and generation of high-energy intermediates upon initial reduction of $N_2$ (e.g., $N_2H$, $N_2H_4$) are major roadblocks to obtaining higher yields.[22–28] A critical factor is that the conduction band of most of the common semiconductors used barely provides the required potential to drive NRR, thus defining a major impediment to solar-driven nitrogen fixation.[19,20] Another issue often encountered in NRR is the competing $H_2$ evolution, especially under acidic pH conditions, thus lowering the overall Faradaic efficiency of NRR.[18–21]

Recently, 2D transition metal dichalcogenides (TMDCs) have drawn tremendous attention owing to their unique electrical, optical, and mechanical properties, including relatively high carrier mobility and tunable bandgaps. 2D-TMDCs have been deemed suitable (and in some instances game-changing) for applications in fields such as catalysis, electronics, photonics, energy storage, and sensing.[29–46] Concerning their structure, 2D-TMDCs are a class of materials with $MX_2$ stoichiometry, where M refers to a transition metal typically from Groups 4 − 7 (M = Ti, Nb, Ta, Mo or W) and X refers to a chalcogen (X = S, Se or Te).[32] 2D-TMDCs possess a hexagonal structure consisting of transition metal atoms on non-neighboring sites covalently bonded to a stacked pair of chalcogen atoms on alternate sites and with a resulting $MX_2$ structural formula. Also, weak van der Waals interactions between adjacent layers of $MX_2$ allow for the delamination of 3D crystals into 2D nanosheets through exfoliation. Exfoliated nanosheets display a surface of chalcogen atoms with the metal atom embedded within the monolayer. The coordination environment of the metal atoms in 2D-TMDCs is most often either octahedral (1 T polymorph) or trigonal prismatic (2H polymorph). The differences in d-orbital splitting cause the polymorphs to display different physical properties, even for materials containing the same $MX_2$ formula. For example, monolayers of 1T-$MoS_2$ are metallic, whereas monolayers of 2H-$MoS_2$ are semiconducting with a direct bandgap of about 1.9 eV.[47] Due to the similarity in their crystal structure and lattice constants, to date, the theoretical prediction of the structures of ~40 different types of TMDCs[31] and syntheses of several $MX_2$ has been possible[48–53] and, critically for our NRR photocatalysis application, allows for continuous bandgap modulation.

It is known that surface vacancies in nanomaterials modify the electronic structure and reduce the coordination of surface atoms, both of which contribute to the formation of dangling bonds, open sites for ligand bonding—particularly critical for notoriously poor electron donor ligands like $N_2$—and enhanced catalytic performance. Moreover, the removal of a chalcogen atom from the

*Electrochemical Society Fellow.
[z]E-mail: Thomas.Cundari@unt.edu; Jeffry.Kelber@unt.edu; Francis.dsouza@unt.edu

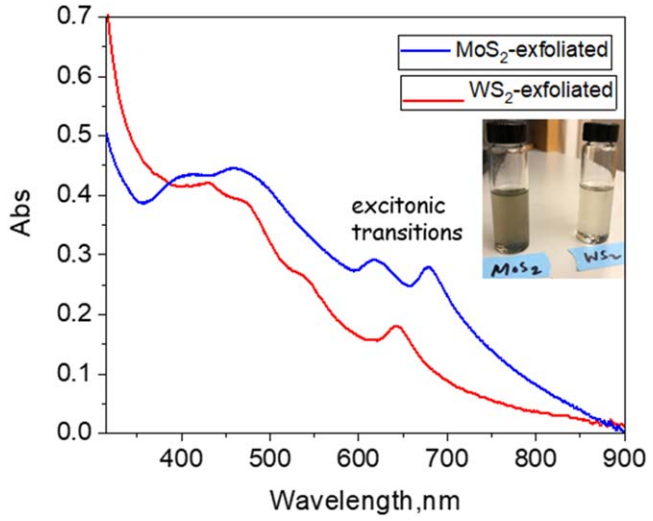


**Figure 1.** The UV-visible spectrum of exfoliated $MoS_2$ (blue) and $WS_2$ (red) in NMP. The inset shows the soluble exfoliated TMDCs.

TMDC nanosheet results in a formal reduction of the transition metal oxidation state, enhancing π-backbonding to $N_2$, which our recent research on oxide/oxynitride systems[54,55] has indicated is a critical factor in binding $N_2$ and activating it for proton-/electron-transfer. Taking advantage of the multi-exciton/trion-forming ability of $MoS_2$, Sun et al.[56] recently demonstrated photochemical NRR using ultrathin $MoS_2$ nanosheets with S vacancies with an ammonia production rate of 325 $\mu$mol $g_{cat}^{-1}$ $h^{-1}$ in deionized water (pH = 3.5), and at the same time demonstrating lack of NRR activity from bulk $MoS_2$ under similar experimental conditions.

Knowing the significance of modified $MoS_2$ for NRR reactions, in the present study, we have extended TMDC electrocatalysis to include another TMDC system, $WS_2$, and developed a procedure to exfoliate y their structures with significant S vacancies. The present results show that both exfoliated $MoS_2$ and $WS_2$, with S vacancies, are electroactive for NRR in the dark, but the addition of visible light excitation results in a very substantial increase in $NH_3$ yield in both materials. As part of this study, we also present direct evidence from femtosecond pump-probe spectroscopy that photoreduction is due to a multi-exciton-driven mechanism involving $N_2$ bound to S vacancies. Also, the experimental data and DFT calculations presented here demonstrate the practical importance of S vacancies as binding/activation sites for $N_2$. The similar NRR behavior of both $MoS_2$ and $WS_2$ suggests that transition metal dichalcogenides (TMDCs) are a class of potential photocatalysts for NRR and similar electro- and photocatalytic applications.

## Experimental

***General.***—All the chemicals were purchased from commercial sources and used without further purification. The UV-visible spectral measurements were carried out with a JASCO V-670 spectrophotometer. Linear and cyclic voltammograms were recorded on an EG&G 263 A electrochemical analyzer using a three-electrode system. A platinum button or surface-coated FTO electrodes were used as the working electrodes. A platinum wire served as the counter electrode and an Ag/AgCl electrode was used as the reference electrode. All the solutions were purged prior to electrochemical and spectral measurements using argon gas.

***Ex-situ XPS.***—Ex situ XPS spectra were acquired in a system with a 100 mm mean radius hemispherical analyzer (VSW Scientific Instruments), with a multi-channel plate detector (PSP Vacuum Technology) using unmonochromated AlKα radiation. The base pressure of this turbomolecularly pumped system was $2 \times 10^{-10}$ Torr. Spectra were acquired at ambient temperature in constant pass energy mode with a pass energy of 50 eV. Photoemission binding energies were calibrated with reference to a Sn $3d_{5/2}$ binding energy of 486.7 eV from the FTO substrate.[57] Spectral deconvolution was carried out by standard methods using Gaussian-Lorentzian functions.[58]

***Gas Chromatography (GC).***—GC experiments were performed on a Shimadzu model GC-2014AT instrument. From calibration, the gas chromatography-thermal conductivity detector (GC-TCD) peak at 2.62 min was attributed to hydrogen while a peak at 3.68 min is attributed to oxygen.

***Femtosecond transient spectroscopy.***—Femtosecond transient absorption spectroscopy experiments were performed using an ultrafast femtosecond laser source (Libra) by Coherent, incorporating a diode-pumped, mode locked Ti:sapphire laser (Vitesse) and a diode-pumped intracavity doubled Nd:YLF laser (Evolution) to generate a compressed laser output of 1.45 W. For optical detection, a Helios transient absorption spectrometer coupled with a femtosecond harmonics generator, both provided by Ultrafast Systems LLC, were used. The sources for the pump and probe pulses were derived from the fundamental output of Libra (Compressed output 1.45 W, pulse width 100 fs) at a repetition rate of 1 kHz; 95% of the fundamental output of the laser was introduced into a TOPAS-Prime-OPA system with a 290 − 2600 nm tuning range from Altos Photonics Inc., (Bozeman, MT), while the rest of the output was used for generation of a white light continuum. Kinetic traces at appropriate wavelengths were assembled from the time-resolved spectral data. Initial data analysis was performed using Surface Xplorer software supplied by Ultrafast Systems. All measurements were conducted in degassed solutions at 298 K. The estimated error in the reported rate constants is ±10%.

***Plane-wave density functional theory simulations.***—All computations were performed using the VASP package (version 5.4.4). All simulations were spin-polarized and implemented PAW and projector-augmented wave methods. Corrections for both dispersion and solvation were included in all simulations. Calculations utilized a plane wave cutoff energy of 500 eV; SCF convergence was considered to be $< 1 \times 10^{-5}$ eV. Surface calculations, done in an asymmetrical unit cell of a = b = 9.56848 Å, c = 32.52951 Å, $\alpha = \beta = 90°$, $\gamma = 120°$, and used a K-point mesh of $3 \times 3 \times 1$.[44,54] Calculations utilized the Methfessel–Paxton method[54,55] with $\sigma$ = 0.2 eV.

***Product analysis.***—For product analysis, a 2 $cm^2$ functionalized TMDC-coated FTO electrode was dipped in 20 ml of 0.1 M sodium sulfate under an $N_2$ atmosphere. The solution pH under these conditions was ∼7.0. Electrolysis was performed in an H-cell with a treated Nafion membrane separating the two compartments at an applied potential of −0.90 V vs Ag/AgCl for 1.5 h. Next, a 10 ml sample of the electrolysis solution was treated with 0.5 ml of 0.55 M NaOH containing 5 wt% salicylic acid and sodium citrate, 100 $\mu$L of sodium nitroprusside dehydrate, and 100 $\mu$L of sodium hypochlorite to generate indophenol blue from the ammonia formed during the bulk hydrolysis experiment.[54,55] After maintaining the solution at room temperature for 15 min, the absorbance of the solution was measured using a JASCO V-670 spectrophotometer. A control experiment using commercial ammonia to produce indophenol blue using the above procedure was also performed. In both cases, the produced indophenol blue revealed similar spectral characteristics.

In a separate experiment, 10 ml of the electrolyte after electrolysis was treated with the working reagent (WR) formed by mixing sodium sulphate (1 g in 125 ml water), borate buffer (80 g in 2 L water), and *ortho*-phthadialdehyde (4 g in 100 ml of ethanol).[59] A control using commercial $NH_3$ was also prepared by a similar procedure. The resultant mixtures were stored in the dark for 1 hour; fluorescence measurements were carried out

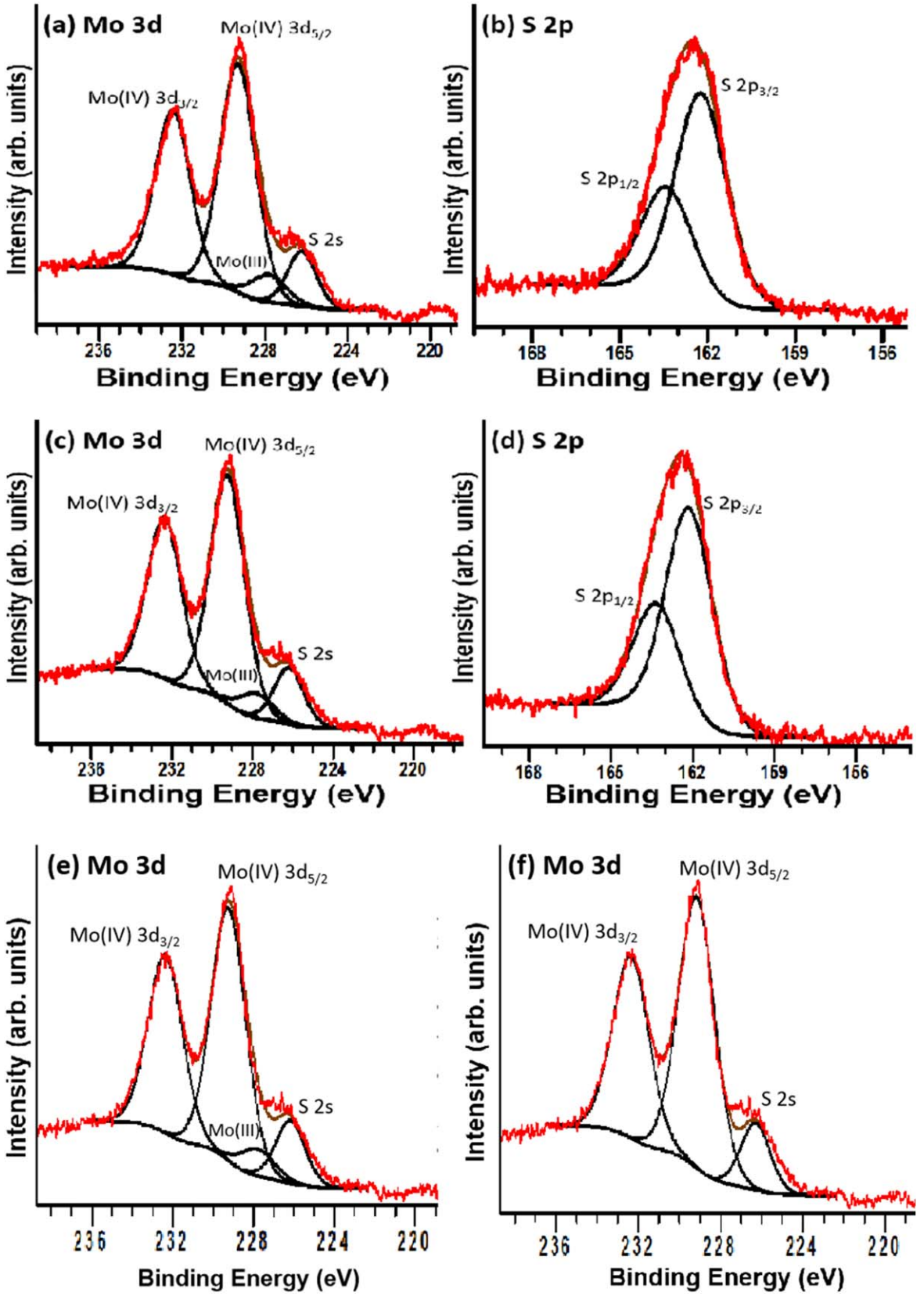


**Figure 2.** Deconvoluted XPS of selected core level peak regions: (a) Mo 3d, exfoliated sample and S 2S, exfoliated $MoS_2$ sample; (b) and (c) corresponding spectra for the bulk $MoS_2$ sample (e) and (f) Deconvoluted Mo3d spectra for bulk $MoS_2$ with and without Mo(III) component respectively.

using a Horiba Jobin Yvon Nanolog UV-visible-NIR spectrofluorometer at the excitation wavelength of 360 nm corresponding to dye absorption.

Hydrazine—another possible by-product of NRR—was detected using the Watt and Chrisp method.[60] The color reagent was first prepared by mixing *para*-$C_9H_{11}NO$ (5.99 g), HCl (30 ml), and

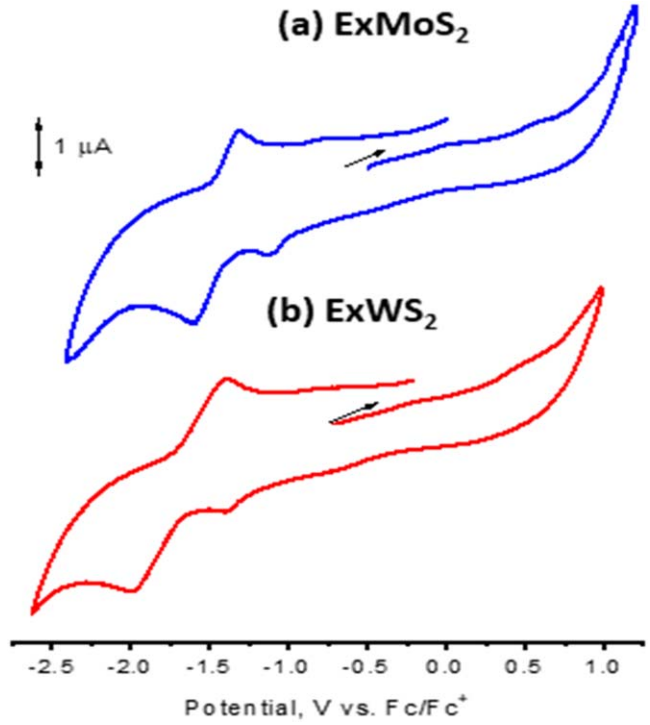


**Figure 3.** Cyclic voltammograms of (a) exfoliated $MoS_2$ and (b) exfoliated $WS_2$ in DMF containing 0.1 (TBA)$ClO_4$. Scan rate = 100 mV $S^{-1}$.

$C_2H_5OH$ (300 ml). After the electrolysis, the solution was added to 9.0 ml of 1.0 M HCl and 5.0 ml of the color reagent with rapid stirring at room temperature. After incubation for 20 min, the absorbance was measured at 455 nm to detect hydrazine.

## Results and Discussion

Samples for this study consisted of exfoliated sheets of commercially available $MoS_2$ and $WS_2$ on fluorinated tin oxide (FTO) substrates. Chlorosulfonic acid was added to bulk TMDC, and the mixture was sonicated to facilitate the exfoliation of the layers.[61] Water was then added with vigorous stirring to cause the thermal decomposition of the superacid, generating large amounts of heat and thereby further helping the exfoliation process. The exfoliated $MoS_2$ and $WS_2$ were soluble in water and organic solvents such as N-methyl pyrrolidine (NMP, see Fig. 1 inset) and dimethylformamide (DMF). In other common organic solvents, the compounds were also initially soluble; however, they started precipitating within 24 h. Please note that with the current exfoliation method, TMDCs of different sizes and thickness exist.

Evidence for exfoliation/functionalized TMDCs retaining their semiconducting 2H-phase was provided by UV-visible absorption spectral studies, Fig. 1. Exfoliated $MoS_2$ revealed characteristic bands at 407 nm and 461 nm arising from direct transitions from the valence to the conduction band (due to the trigonal prismatic semiconducting 2H-phase), and at 619 nm and 678 nm due to excitonic transitions. The nicely resolved excitonic peaks, resembling those derived from mechanically exfoliated monolayer $MoS_2$,[62–67] support the existence of an ordered 2H structure. Similarly, the absorption spectrum of exfoliated $WS_2$ also supported the retention of the 2H-phase. For the tungsten material, the characteristic excitonic band was located at 638 nm, while the indirect excitonic transition was located at 531 nm. Direct transition bands were located at 422 nm and 466 nm, evidence of semiconducting character with a direct bandgap.[62–67] The nicely-developed and resolved spectral peaks in the case of both exfoliated $MoS_2$ and $WS_2$ confirmed that the current exfoliation/functionalization

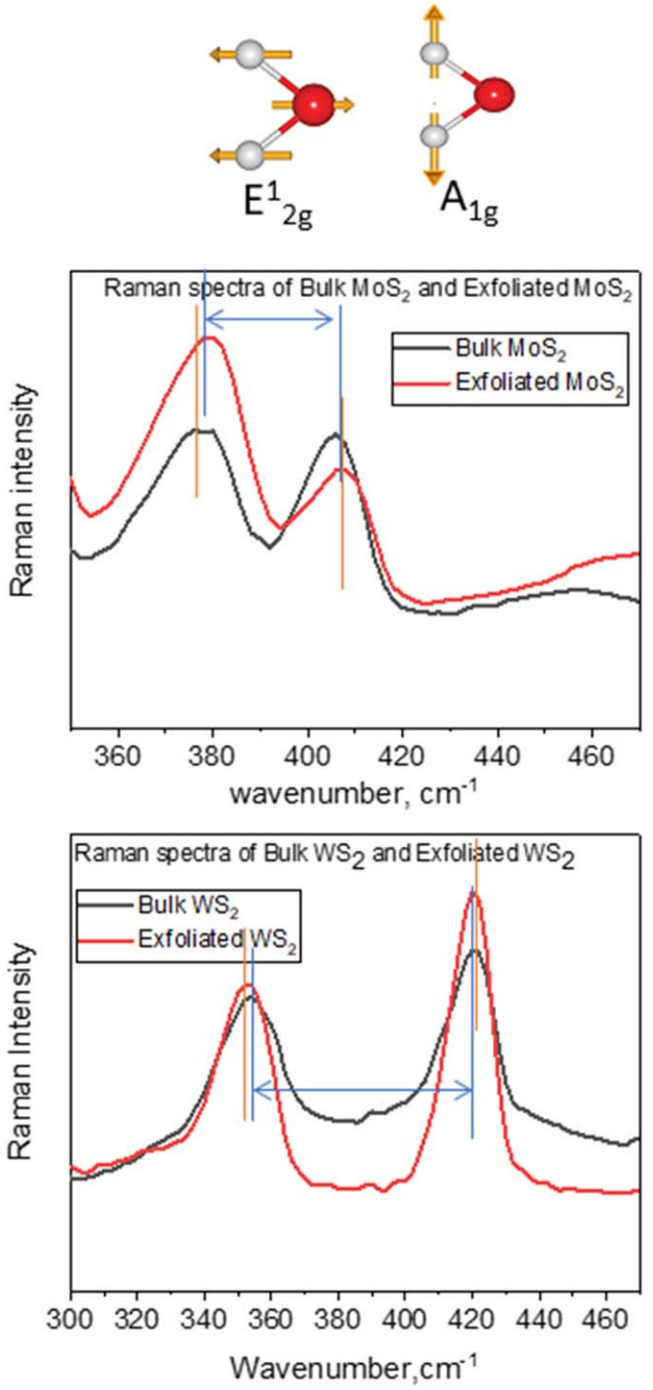


**Figure 4.** Raman spectra of the indicated bulk (black) and exfoliated (red) TMD materials; (top) $MoS_2$, (bottom) $WS_2$.

procedure did not compromise the basic semiconductor properties of the employed TDMCs.

XPS spectra of bulk and exfoliated $MoS_2$ samples were acquired to determine the extent of possible S vacancies, Mo oxidation, and if the samples were in the semiconducting 2H phase or the metallic 1 T phase. Mo 3d and S 2p core level spectra for the exfoliated $MoS_2$ sample are shown in Figs. 2a and 2b, respectively. As shown in Figs. 2a and 2b, the exfoliated sample displayed Mo $3d_{5/2}$ and Mo $3d_{3/2}$ binding energies of 229.2 eV and 232.4 eV, respectively, with S $2p_{3/2}$ and S $2p_{1/2}$ binding energies of 162.4 eV and 163.4 eV, respectively. These binding energies correspond closely to those reported for the semiconducting 2H phase of $MoS_2$.[65] Importantly, there is no evidence in Fig. 2 of Mo(VI), which would correspond to

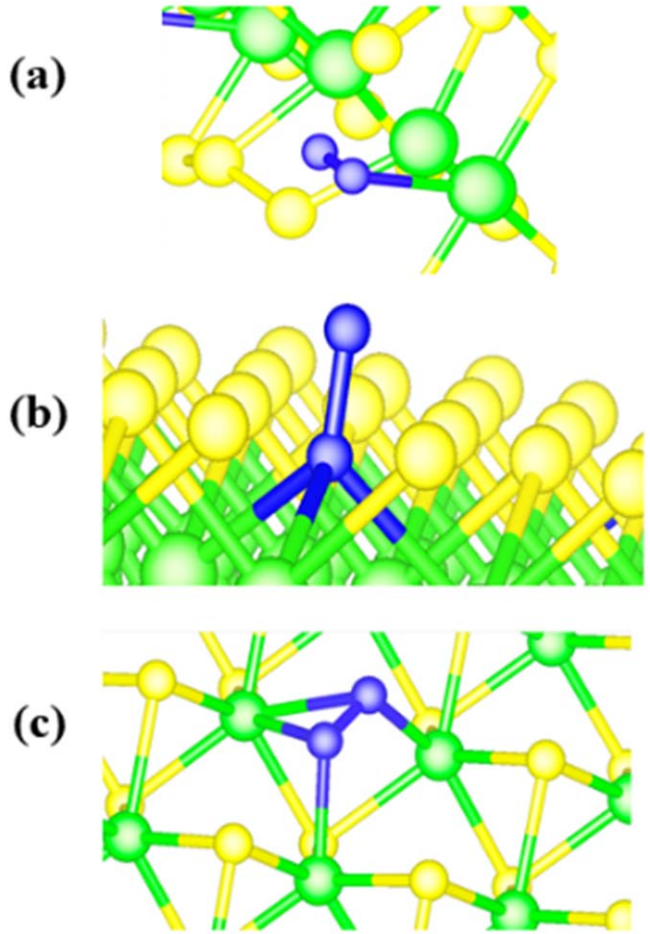


**Figure 5.** DFT optimized structures of $N_2$ (blue) bound to S vacancies of 2H-$MoS_2$ (a) edge, (b) $\mu^3$, and (c) bridging linkage isomers. Metal, S and N atoms are represented by green, yellow and blue spheres, respectively.

a Mo $3d_{3/2}$ spectral intensity near 236 eV.[65] For the Mo 3d peak, 5 components were added for deconvolution. The first two were for Mo(IV) $3d_{5/2}$ and Mo(III) $3d_{3/2,}$ respectively, which are expected for stoichiometric $MoS_2$. A third and fourth peak was added for Mo(III) $3d_{5/2}$ and Mo(III) $3d_{3/2,}$ respectively, which accounted for Mo atoms adjacent to S vacancies. The fifth peak was added to account for the overlap of the S 2 s peak positioned at a lower binding energy than the Mo components.

The Mo $3d_{5/2}$ spectra for both exfoliated (Fig. 2a) and bulk (Fig. 2b) both exhibit significant Mo(III)$3d_{5/2}$ components. This indicates that both samples contain S vacancies. Estimating Mo(III)$3d_{5/2}$/Mo(IV)$3d_{5/2}$ intensity ratio yields 0.11 and 0.12 for the bulk and exfoliated samples, respectively. This indicates a slightly higher concentration of S vacancies in exfoliated, relative to the bulk sample.[68] In principle, the elemental composition of a homogenous sample can be determined from XPS core level spectra according to:

$$Mo = \frac{I_S/ASF_S}{I_{Mo}/ASF_{Mo}} \quad [1]$$

In Eq. 1, $I_S$ is the integrated peak intensity for the S $2p_{3/2}$ and $2p_{1/2}$ components, while $I_{Mo}$ includes $3d_{5/2}$ intensities for both Mo (III) and Mo(IV) components, and $ASF_{S,Mo}$ is the corresponding atomic sensitivity factors appropriate to this analyzer for the Mo $3d_5/_2$ and $S_{2p}$ features—the latter including both (unresolved) $2p_{3/2}$ and $2p_{1/2}$ components.[69] Using those atomic sensitivity factors yields a S/Mo atomic ratio of 2.1. However, such "nominal" sensitivity factors are often inaccurate by as much as 10% due to variations in inelastic mean free paths and other factors.[69] Scaling the ratio of atomic sensitivity factors to yield a Mo/S atomic ratio of 1.9 for the bulk sample (appropriate on the basis of Mo(III)/Mo(IV) intensity ratios) yields an estimated S/Mo atomic ratio of ∼1.8 for the exfoliated sample.

In summary, both exfoliated and bulk $MoS_2$ exhibit S vacancies amounting to ∼10% of Mo sites, with a slightly higher concentration in the exfoliated sample.

Both exfoliated $MoS_2$ and $WS_2$ were electroactive. The cyclic voltammograms (CVs) of exfoliated $MoS_2$ and $WS_2$ in DMF containing 0.1 M (TBA)$ClO_4$ are shown in Fig. 3. Exfoliated $MoS_2$ revealed irreversible oxidations at $E_{pa} = -0.08$ and 0.48 V and quasi-reductions at $E_{pc} = -1.20$ and $-1.69$ V vs $Fc/Fc^+$. Similarly, the exfoliated $WS_2$ revealed irreversible oxidations at $E_{pa} = 0.23$ and 0.44 V and quasi-reversible reductions at $E_{pc} = -1.40$ and $-1.98$ V.[70] From this study, facile oxidation, and reduction of both $MoS_2$ and $WS_2$ were demonstrated, indicating a smaller bandgap and easier oxidation/reduction processes of $MoS_2$ vs $WS_2$.

XPS results indicating exfoliated sheets of 2H-$MoS_2$ and 2H-$WS_2$ (Fig. 2) were confirmed by Raman spectra excited by 532 nm radiation (Fig. 4). In the case of exfoliated $MoS_2$, spectral measurements upon 532 nm excitation revealed two strong Raman bands, deconvoluted by a single Lorentzian centered at 384.1 $cm^{-1}$ and 410 $cm^{-1}$, and were assigned to in-plane $E^1_{2g}$ and out-of-plane$A_{1g}$ vibrational modes (Fig. 5).[71–75] The frequency difference between $A_{1g}$ and $E^1_{2g}$ peaks was 25.9 $cm^{-1}$, which is reduced in comparison to the value derived from the bulk material (ca. 28.5 $cm^{-1}$), thus signifying the success of our exfoliation procedure and the existence of 2H-$MoS_2$ nanosheets that are a few layers thick.[61] Similarly, for exfoliated 2H-$WS_2$, intense Raman bands centered at 353.9 $cm^{-1}$ and 419.9 $cm^{-1}$ assigned to the $E^1_{2g}$ and $A_{1g}$ modes, respectively, were evident.[71,72] The peak-to-peak separation of 65.9 $cm^{-1}$—compared with a value of 67.13 $cm^{-1}$ for the bulk material—suggests the presence of few-layer materials in this case also. Acquisition of the spectra at different locations of the samples revealed the peak positions and their full width at half maxima (FWHM) to be identical, thus revealing high homogeneity for exfoliated TMDCs. In summary, the Raman studies provided no evidence of major structural damage and/or covalent bond formation as a result of chlorosulfonic acid treatment of the semiconducting TMDCs.

Plane-wave density functional theory calculations incorporating solvation and dispersion effects were performed using procedures described previously,[54,55,76] to investigate S vacancy effects on $N_2$ binding and N≡N bond activation. The results showed preferred $N_2$ binding to edge site S vacancies (Fig. 5a), in agreement with the literature.[77,78] Calculations performed on pristine $MoS_2$ surface models without S vacancies revealed a lack of $N_2$ binding. The calculations also indicated strong $N_2$ adsorption at *surface* single and double S vacancies (Fig. 5b), with calculated NN bond elongation of 1.198 Å and 1.216 Å for $\mu^3$-$N_2$ bound to single and double surface vacancies, respectively, vs 1.109 Å for gaseous $N_2$ at the same level of theory. Marginally higher in energy is another isomer in which each N of dinitrogen is bound to two metal ions (Fig. 5c); $r_{NN}$ is even further elongated from 1.198 to 1.230 Å (single $S_{vac}$) in the isomer. The very long N-N bond length ($r_{NN}$) for exfoliated $MoS_2$ is encouraging concerning NN bond activation and scission.[54,55,76] Bader population analysis indicates that an extra $\sim^1/_4$ $e^-$ is donated into $N_2$ when it is bound to the double vs a single vacancy, consistent with the longer NN bond length. Calculations indicate a reduction of the work function of ∼0.2 eV for exfoliated $MoS_2$ upon introduction of even a small percentage of vacancies, e.g., $MoS_{1.8}$, suggesting S-vacancies make TMDCs more adept at $\pi$-backbonding, which our research indicates is essential for activation and protonation of $*N_2$ to form the critical *NNH intermediate.[54,55,76] Another herald of NRR activity for these TMDCs is the downhill energy change for $N_2$ scission, calculated thusly, $S_{vac}$-$N_2 + {}^3/_2\ H_2 \rightarrow S_{vac}N + NH_3$, which is significantly downhill, −61.5 kcal $mol^{-1}$.

The above DFT results support $N_2$ binding at S-vacancy sites of exfoliated $MoS_2$ and the prediction that excitons and trions

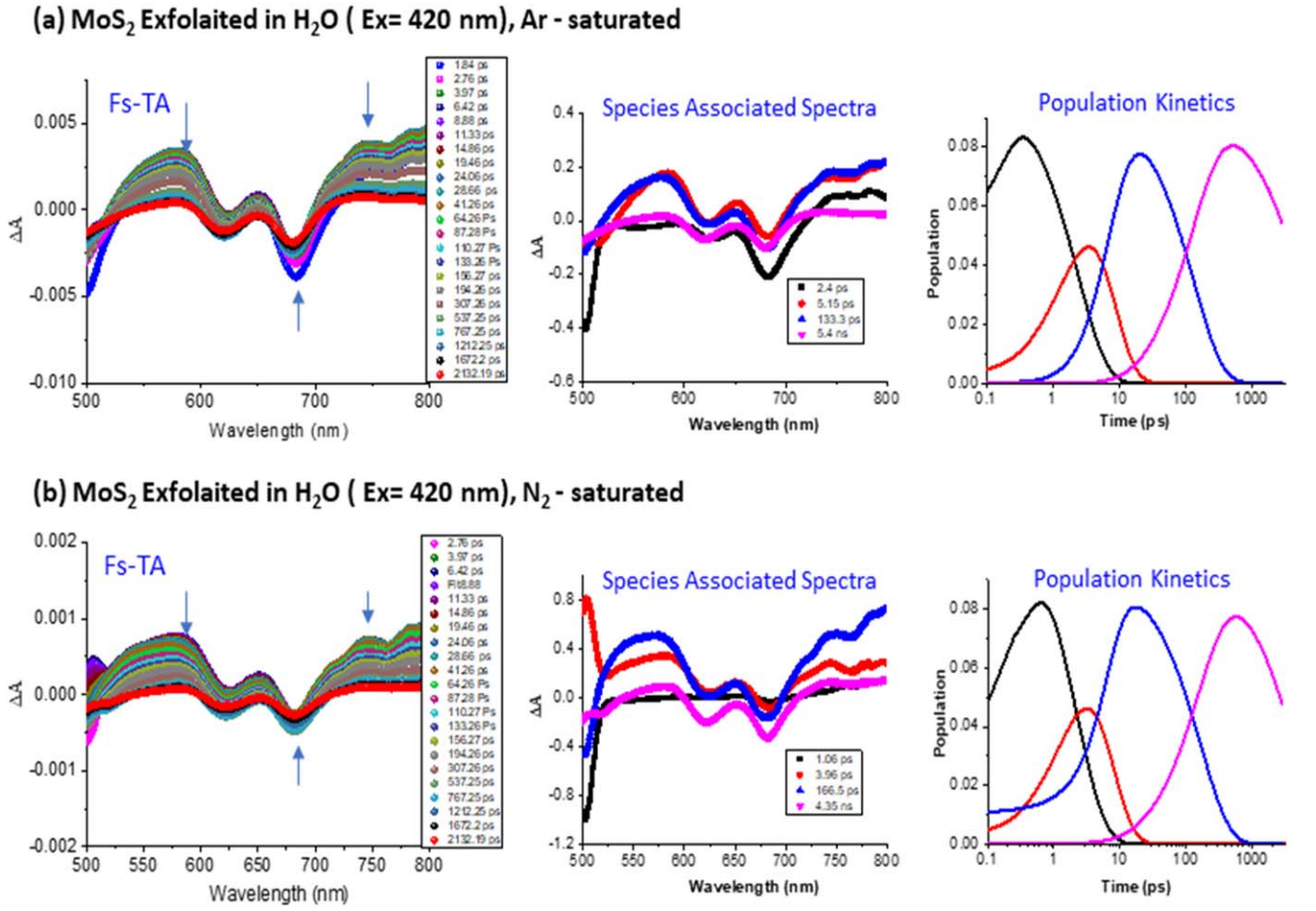


**Figure 6.** Fs-TA spectra at the indicated delay times of exfoliated $MoS_2$ in (a) Ar-saturated, and (b) $N_2$-saturated water. The samples were excited at 420 nm (100 fs pulses). The middle panel shows SAS from GloTarAn analysis, and the right panel shows the population kinetics of different species.

generated upon photoexcitation can pump electrons into bound $N_2$. To secure further evidence for this process, the excited state events were probed by femtosecond transient absorption (fs-TA) spectroscopy on exfoliated $MoS_2$. For this study, DMF was chosen as the solvent due to the appreciable solubility of exfoliated $MoS_2$, which was excited at 420 nm (100 fs pulses). A lowering of the lifetime of excitons and trions is expected if the excitons/trions generated upon photoexcitation interact with the bound $N_2$, as the bound adsorbate offers another photochemical deactivation path. The key findings are summarized in Fig. 6. It may be mentioned here that the $N_2$-bound TMDCs would not result in different optical signature peaks in the visible-near IR region compared to pristine TMDC. Hence, evidence for $N_2$ interaction could only be secured from their kinetic plots.

As shown in Fig. 6a, in the case of exfoliated $MoS_2$ in Ar-saturated water, the excited state of ex$MoS_2$ formed within the first 2 ps, revealing three minima at 502, 620, and 684 nm due to excitonic transitions in the absorption spectrum, and two maxima at 578 and 650 nm corresponding to induced absorption of B and A excitons.[77,79] During the first 5 − 6 ps, all peaks experienced a small blue shift ascribed to cooling of hot excitons and/or inter-excitonic interactions. Decay/recovery of the positive/negative peaks did not develop any new peaks within the monitoring window of 3 ns. Interestingly, when the solution was saturated with $N_2$, the main transitions persisted, but with subtle changes (Fig. 6b). In this instance, the excitonic transition minima were located at 500 nm, 622 nm, and 682 nm, and the induced absorption peaks at 575 nm and 652 nm. Importantly, the decay/recovery of the positive/negative peaks revealed the development of a new peak at 504 nm by ∼10 ps, and a new shoulder-type peak at ∼540 nm. Further, the transient data were subjected to Global Target Analysis,[80] and the species-associated spectra (SAS) and population kinetics for major transient species were generated (middle and right-hand panels of Fig. 6). Under both experimental conditions, the data yielded four SAS components corresponding to excited state and various excitonic states (e.g., exciton, trion). Most importantly, time constants from population kinetics (average lifetime of a given species) were significantly lower in the presence of $N_2$ as compared to the corresponding values in Ar (2.40 ps, 5.15 ps, 133 ps, and 5.4 ns for Ar-saturated solution vs 1.06 ps, 3.96 ps, 16.6 ps, and 4.35 ns for $N_2$-saturated solution). To our knowledge, these results provide the first proof of the interaction of an exciton/trion with bound $N_2$ at the exfoliated $MoS_2$ surface.

Having demonstrated $N_2$ binding to exfoliated TMDC materials and the interaction of photochemically generated excitons/trions with bound nitrogen, attention was next focused on the ability of the exfoliated TMDCs to undergo NRR reactions under electrocatalytic and photocatalytic conditions.

Linear scan voltammograms (LSVs) of exfoliated $MoS_2$ and $WS_2$ (Figs. 7a and 7b, respectively) were recorded under different experimental conditions in water containing 0.1 M $Na_2SO_4$ supporting electrolyte at pH = 7 by placing the electrode in a sealed 1 cm quartz cuvette.[81,82] Endurance tests were performed by multicyclic voltammetry (15 cycles). Ammonia formation was performed by bulk-electrolysis at a given applied potential (−0.55 to −0.65 V vs Ag/AgCl depending on the TMDC material), and by generating indophenol blue using catalytically produced $NH_3$, which was subsequently quantified by optical absorption.[54,55] The $N_2$ gas used to purge the sample was passed through two traps, the first containing 0.1 M HCl, and the second 0.1 M KOH, to remove trace amounts of ammonia or nitride/nitrite contaminants. Precautions

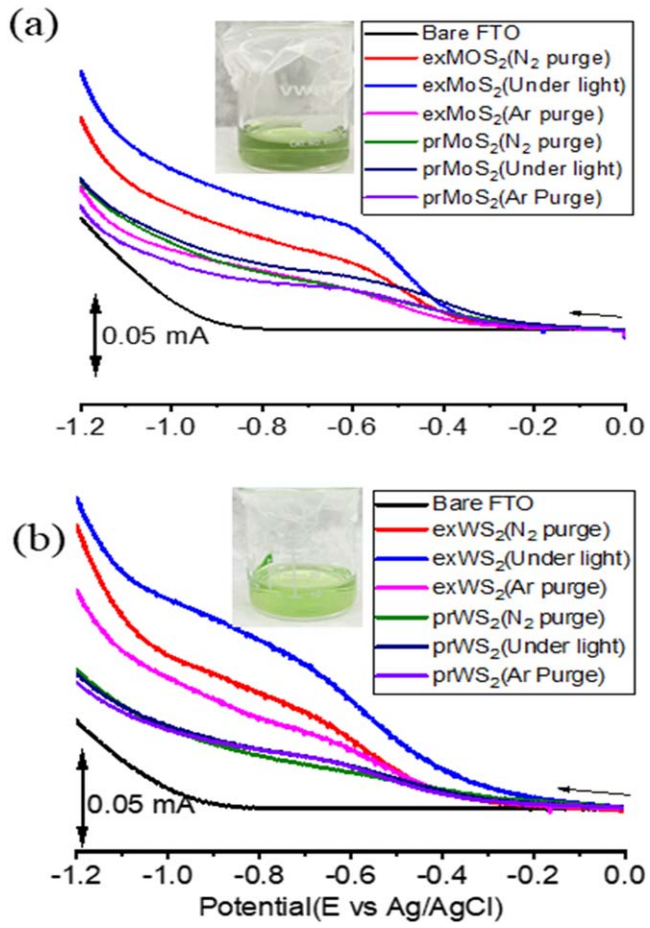


**Figure 7.** linear scan voltammograms (LSVs) of pristine/bulk (pr) and exfoliated (ex) (a) $MoS_2$ and (b) $WS_2$ under dark and light (AM 1.5) illumination conditions and in Ar and $N_2$ atmospheres in water containing 0.1 M $Na_2SO_4$ (pH ~ 7.0). Figure insets show the colour of indophenol blue generated from ammonia produced from bulk electrolysis under light-illumination conditions.

were exercised to avoid contaminations of $NH_3$ from air and breath entering the reaction vessel. Experiments under light conditions were performed using a solar simulator at AM1.5 conditions.

The results (Fig. 7) show that exfoliated (ex) $MoS_2$ (Fig. 7a) and exfoliated $WS_2$ (Fig. 7b) exhibit substantially higher currents than corresponding pristine/bulk (pr) samples. In the single compartment cell, the Faradaic efficiency and $NH_3$ yield rate were found to be 1.08% and 20.80 $\mu molg^{-1}h^{-1}$ in dark vs 1.14% and 21.87 $\mu molg^{-1}h^{-1}$ under light for $MoS_2$; and 0.72% and 16.00 $\mu molg^{-1}h^{-1}$ in the dark vs 0.91% and 18.60 $\mu molg^{-1}h^{-1}$ under light for $WS_2$, respectively. For each exfoliated sample, 2 − 3 times higher currents are observed in the presence of visible light, and in the presence of $N_2$, vs Ar-saturated electrolyte, consistent with $NH_3$ formation. The production of $NH_3$ under visible light conditions was, in each case, confirmed by UV absorption measurements using indophenol blue (see Fig. S1 in SI for optical spectra and pertinent equations) and fluorescence spectroscopic methods (see Fig S2). The Faradaic efficiency was found to be 1.18% in dark and 1.26% under light for $MoS_2$; and 0.68% in the dark vs 0.85% under light for $WS_2$, respectively. It is important to note that the results from both these methods were in agreement with the experimental error. A control experiment was also performed on bare FTO without coated TMDC material both under $N_2$ and Ar atmosphere. No measurable $NH_3$ was detected suggesting that the $NH_3$ produced in Fig. 7 is due to the coated TMDC catalyst on the electrode surface. Furthermore, the same experiments were repeated in an H-cell using a Nafion membrane separator. The Faradaic efficiency and $NH_3$ yield rate were found to be 4.85% and 206.04 $\mu molg^{-1}h^{-1}$ in dark vs 5.12% and 226.66 $\mu molg^{-1}h^{-1}$ under light for $MoS_2$; and 4.07% and 159.72 $\mu molg^{-1}h^{-1}$ in the dark vs 4.45% and 179.88 $\mu molg^{-1}h^{-1}$ under light for $WS_2$, respectively. GC analyses of product mixtures were also performed but revealed no measurable $H_2$ formation in the NRR product of $MoS_2$ and $WS_2$ samples (see Fig. S3). Additionally, spectroscopic tests were performed to detect any hydrazine formation during the process of NRR (see the experimental section for details). Such tests revealed the absence of hydrazine as a by-product in both exfoliated TMDC materials (see Fig. S4). Importantly, electrochemical and much-improved photoelectrocatalytic NRR activity of exfoliated TMDCs has been demonstrated. Current-time switching and light ON-OFF experiments reveal the robust nature and ON-OFF switchability (see Fig. S5) of these catalysts, without appreciable degradation of the catalysts, for several hours.

## Conclusions

In summary, the exciting findings of this research reveal the following. (i) chlorosulfonic acid treatment of bulk TMDs not only exfoliated them into a few layers but also created S-vacancies (mainly at the edges) on the order of ~10%, as determined by XPS studies. (ii) Optical absorption and Raman, studies on exfoliated TMDCs revealed the preservation of semiconducting (2H-phase) properties of the exfoliated TMDCs. (iii) DFT calculations supported $N_2$ binding to exfoliated $MoS_2$ at S-vacancy sites with substantial electron donation to the dinitrogen substrate. (iv) Fs-TA spectral studies provided evidence for the generation of excitons/trions upon photoexcitation of exfoliated $MoS_2$ and their interaction with bound $N_2$. (v) LSVs recorded on modified electrodes revealed higher NRR activity for exfoliated TMDC-modified electrodes, and such activity was 2–3 higher in the presence of light illumination. (vi) Bulk electrolysis followed by spectral measurements of indophenol produced from generated $NH_3$, confirmed ammonia to be the main product of electrocatalytic and photocatalytic NRR. No measurable $H_2$ could be detected under both dark and light-illumination conditions. Further studies to optimize the experimental conditions for enhanced NRR yields and to probe pertinent mechanistic aspects and the effect of pH and supporting electrolytes are underway in our laboratories.

## Acknowledgments

The authors gratefully acknowledge the support of this work by the National Science Foundation through the grant DMR-2112864. Additional NSF support for the UNT CASCaM HPC cluster via Grant CHE-1531468 is also gratefully acknowledged. T.R.C. also thanks the NSF for partial support of this research via grant CHE-1953547.

## Notes and references

Supporting Information (SI) available: Absorption and fluorescence spectra for $NH_3$ and hydrazine detection on bulk electrolysis products, GC traces for $H_2$ detection and current-voltage plots under light on-off conditions.

## ORCID

Francis D'Souza https://orcid.org/0000-0003-3815-8949

## References

1. X. Xue, R. Chen, C. Yan, P. Zhao, Y. Hu, W. Zhang, S. Yang, and Z. Jin, *Nano Res.*, **11**, 2992 (2018).
2. H. Ali, M. Masar, A. C. Guler, M. Urbanek, M. Machovsky, and I. Kuritka, *Nanoscale Adv.*, **3**, 6358 (2021).
3. S. Chen, D. Liu, and T. Peng, *Sol. RRL*, **5**, 2000487 (2020).
4. R. Shi, X. Zhang, G. I. N. Waterhouse, Y. Zhao, and T. Zhang, *Adv. Energy Mater.*, **10**, 2000659 (2020).
5. H. Jin, C. Guo, X. Liu, J. Liu, A. Vasileff, Y. Jiao, Y. Zheng, and S.-Z. Qiao, *Chem. Rev.*, **118**, 6337 (2018).
6. X. Z. Chen, N. Li, Z. Kong, W.-J. Ong, and X. Zhao, *Mater. Horiz.*, **5**, 9 (2018).
7. X. Cui, C. Tang, and Q. Zhang, *Adv. Energy Mater.*, **8**, 1800369 (2018).
8. M. A. Shipman and M. D. Symes, *Catal. Today*, **286**, 57 (2017).

9. J. W. Erisman, M. A. Sutton, J. Galloway, Z. Klimont, and W. Winiwarter, *Nat. Geosci.*, **1**, 636 (2008).
10. R. Schlögl, *Angew. Chem. Int. Ed.*, **42**, 2004 (2003).
11. Y. Tanabe and Y. Nishibayashi, *Coord. Chem. Rev.*, **257**, 2551 (2013).
12. H. Tanaka, A. Sasada, T. Kouno, M. Yuki, Y. Miyake, H. Nakanishi, Y. Nishibayashi, and K. Yoshizawa, *J. Am. Chem. Soc.*, **133**, 3498 (2011).
13. J. A. Pool, E. Lobkovsky, and P. J. Chirik, *Nature*, **427**, 527 (2004).
14. T. Shima, S. Hu, G. Luo, X. Kang, Y. Luo, and Z. Hou, *Science*, **340**, 1549 (2013).
15. H.-P. Jia and E. A. Quadrelli, *Chem. Soc. Rev.*, **43**, 547 (2014).
16. T. A. Bazhenova and A. E. Shilov, *Coord. Chem. Rev.*, **144**, 69 (1995).
17. H. Tanaka, H. Mori, H. Seino, M. Hidai, Y. Mizobe, and K. Yoshizawa, *J. Am. Chem. Soc.*, **130**, 9037 (2008).
18. J. Soria, J. C. Conesa, V. Augugliaro, L. Palmisano, M. Schiavello, and A. Sclafani, *J. Phys. Chem.*, **95**, 274 (1991).
19. D. Zhu, L. Zhang, R. E. Ruther, and R. J. Hamers, *Nat. Mater.*, **12**, 836 (2013).
20. J. R. Christianson, D. Zhu, R. J. Hamers, and J. R. Schmidt, *J. Phys. Chem. B*, **118**, 195 (2013).
21. N. Bauer, *J. Phys. Chem.*, **64**, 833 (1960).
22. A. E. Shilov, *Russ. Chem. Bull.*, **52**, 2555 (2003).
23. J. Li, H. Li, G. Zhan, and L. Zhang, *Acc. Chem. Res.*, **50**, 112 (2017).
24. L. Li, Y. Wang, S. Vanka, X. Mu, Z. Mi, and C.-J. Li, *Angew. Chem.*, **129**, 8827 (2017).
25. H. Li, J. Li, Z. Ai, F. Jia, and L. Zhang, *Angew. Chem. Int. Ed.*, **122** (2018).
26. S. Giddey, S. P. S. Badwal, and A. Kulkarni, *Int. J. Hydrogen Energy*, **38**, 14576 (2013).
27. M. Jewess and R. H. Crabtree, *ACS Sustainable Chem. Eng.*, **4**, 5855 (2016).
28. A. R. Singh, B. A. Rohr, J. A. Schwalbe, M. Cargnello, K. Chan, T. F. Jaramillo, I. Chorkendorff, and J. K. Nørskov, *ACS Catal.*, **7**, 706 (2017).
29. D. Jariwala, V. K. Sangwan, L. J. Lauhon, T. J. Marks, and M. C. Hersam, *ACS Nano*, **8**, 1102 (2014).
30. S. Balendhran, S. Walia, H. Nili, J. Z. Ou, S. Zhuiykov, R. B. Kaner, S. Sriram, M. Bhaskaran, and K. Kalantar-zadeh, *Adv. Funct. Mater.*, **23**, 3952 (2013).
31. Y. Sun, K. Fujisawa, Z. Lin, Y. Lei, J. S. Mondschein, M. Terrones, and R. E. Schaak, *J. Am. Chem. Soc.*, **139**, 11096 (2017).
32. X. Zhu, N. R. Monahan, Z. Gong, H. Zhu, K. W. Williams, and C. A. Nelson, *J. Am. Chem. Soc.*, **137**, 8313 (2015).
33. R. Lv, J. A. Robinson, R. E. Schaak, D. Sun, Y. Sun, T. E. Mallouk, and M. Terrones, *Acc. Chem. Res.*, **48**, 56 (2015).
34. B. Radisavljevic, A. Radenovic, J. Brivio, V. Giacometti, and A. Kis, *Nat. Nanotech.*, **6**, 147 (2011).
35. J. A. Wilson, F. J. Di Salvo, and S. Mahajan, *Adv. Phys.*, **24**, 117 (1975).
36. B. Sipos, A. F. Kusmartseva, A. Akrap, H. Berger, L. Forró, and E. Tutis, *Nat. Mater.*, **7**, 960 (2008).
37. H. Zeng, J. Dai, W. Yao, D. Xiao, and X. Cui, *Nat. Nanotech.*, **7**, 490 (2012).
38. K. F. Mak, K. He, C. Lee, G. H. Lee, J. Hone, T. F. Heinz, and J. Shan, *Nat. Mater.*, **12**, 207 (2013).
39. A. Ramasubramaniam, *Phys. Rev. B*, **86**, 115409 (2012).
40. O. Lopez-Sanchez, D. Lembke, M. Kayci, A. Radenovicand, and A. Kis, *Nat. Nanotech.*, **8**, 497 (2013).
41. M. Fontana, T. Deppe, A. K. Boyd, M. Rinzan, A. M. Liu, M. Paranjape, and P. Barbara, *Sci. Rep.*, **3**, 1634 (2013).
42. M. Bernardi, M. Palummo, and J. C. Grossman, *Nano Lett.*, **13**, 3664 (2013).
43. T. F. Jaramillo, K. P. Jorgensen, J. Bonde, J. H. Nielsen, S. Horch, and I. Chorkenorff, *Science*, **317**, 100 (2007).
44. D. Voiry et al., *Nat. Mater.*, **12**, 850 (2013).
45. M. A. Lukowski, A. S. Daniel, F. Meng, A. Forticaux, L. Li, and S. Jin, *J. Am. Chem. Soc.*, **135**, 10274 (2013).
46. D. Voiry, M. Salehi, R. Silva, T. Fujita, M. Chen, T. Asefa, V. B. Shenoy, G. Eda, and M. Chhowalla, *Nano Lett.*, **13**, 6222 (2013).
47. J. Ryou, Y.-S. Kim, S. KC, and K. Cho, *Sci. Rep.*, **6**, 29184 (2016).
48. Z. Lin, M. T. Thee, A. L. Elías, S. Feng, C. Zhou, K. Fujisawa, N. Perea-López, V. Carozo, H. Terrones, and M. Terrones, *APL Mater.*, **2**, 092514 (2014).
49. J. Mann et al., *Adv. Mater.*, **26**, 1399 (2014).
50. L. Yang, C. Xie, J. Jin, R. N. Ali, C. Feng, P. Liu, and B. Xiang, *Nanomaterials*, **8**, 463 (2018).
51. S. Zheng, L. Sun, T. Yin, A. M. Dubrovkin, F. Liu, Z. Liu, Z. X. Shen, and H. J. Fan, *Appl. Phys. Lett.*, **106**, 063113 (2015).
52. H. Li et al., *J. Am. Chem. Soc.*, **137**, 5284 (2015).
53. Y. Chen et al., *Nanoscale*, **6**, 2833 (2014).
54. A. Ganesan, A. Osonkie, P. Chukwunenye, T. R. Cundari, F. D'Souza, and J. A. Kelber, *J. Electrochem. Soc.*, **168**, 026504 (2021).
55. A. Osonkie, A. Ganesan, P. Chukwunenye, F. Anwar, K. Balogun, M. Gharee, I. Rashed, T. R. Cundari, F. D'Souza, and J. A. Kelber, *ACS Adv. Mater & Interface*, **14**, 531 (2021).
56. S. Sun, X. Li, W. Wang, L. Zhang, and X. Sun, *Appl. Catal. B.*, **200**, 323 (2017).
57. W. Xia, H. Wang, X. Zeng, J. Han, J. Zhu, M. Zhou, and S. Wu, *CrystEngComm*, **16**, 6841 (2014).
58. M. P. Seah and D. Briggs, "Practical surface analysis." *Auger and X-ray Photoelectron Spectroscopy* (NY)(Wiley and Sons) 2nd ed., Vol. 1 (1990).
59. R. M. Holmes, A. Aminot, R. Kérouel, B. A. Hooker, and B. J. A. Peterson, *Canadian J. Fisheries and Aquatic Sciences*, **56**, 1801 (1999).
60. S. Kang, J. Wang, S. Zhang, C. Zhao, G. Wang, W. Cai, and H. Zhang, *Electrochem. Commun.*, **100**, 90 (2019).
61. G. Pagona, C. Bittencourt, R. Arenal, and N. Tagmatarchis, *Chem. Commun.*, **51**, 12950 (2015).
62. B. J. Carey, T. Daeneke, E. P. Nguyen, Y. Wang, J. Z. Ou, S. Zhuiykov, and K. Kalantar-zadeh, *Chem. Commun.*, **51**, 3770 (2015).
63. A. Splendiani, L. Sun, Y. Zhang, T. Li, J. Kim, C.-Y. Chim, G. Galli, and F. Wang, *Nano Lett.*, **10**, 1271 (2010).
64. K. F. Mak, C. Lee, J. Hone, J. Shan, and T. F. Heinz, *Phys. Rev. Lett.*, **105**, 136805 (2010).
65. Y. Yu, C. Li, Y. Liu, L. Su, Y. Zhang, and L. Cao, *Sci. Rep.*, **3**, 1866 (2013).
66. W. Zhao, Z. Ghorannevis, L. Chu, M. Toh, C. Kloc, P.-H. Tan, and G. Eda, *ACS Nano*, **7**, 791 (2013).
67. G. Eda, H. Yamaguchi, D. Voiry, T. Fujita, M. Chen, and M. Chhowalla, *Nano Lett.*, **11**, 5111 (2011).
68. F. D. Brandao, G. M. Ribeiro, P. H. Vaz, J. C. Gonzalez, and K. Krambrock, *J. Appl. Physics*, **119**, 235701 (2016).
69. J. R. Shallenberger, N. J. Smith, and J. Banerjee, *Surf. Interface Anal.*, **53**, 569 (2021).
70. L. Vallan, R. Canton-Vitoria, H. B. Gobeze, Y. Jang, R. Arenal, A. M. Benito, W. K. Maser, F. D'Souza, and N. Tagmatarchis, *J. Am. Chem. Soc.*, **140**, 13488 (2018).
71. C. Lee, Q. Li, W. Kalb, X.-Z. Liu, H. Berger, R. Carpick, and J. Hone, *Science*, **328**, 76 (2010).
72. S. Ghatak, A. N. Pal, and A. Ghosh, *ACS Nano*, **5**, 7707 (2011).
73. H. Li, Q. Zhang, C. C. R. Yap, B. K. Tay, T. H. T. Edwin, A. Olivier, and D. Baillargeat, *Adv. Funct. Mater.*, **22**, 1385 (2012).
74. S.-L. Li, H. Miyazaki, H. Song, H. Kuramochi, S. Nakaharai, and K. Tsukagoshi, *ACS Nano*, **6**, 7381 (2012).
75. H. Terrones et al., *Sci. Rep.*, **4**, 4215 (2014).
76. P. Chukwunenya, A. Ganesan, M. Gharaee, K. Balogun, F. Anwar, Q. Adesope, T. R. Cundari, F. D'Souza, and J. A. Kelber, *J. Mater. Chem. A*, **10**, 21401 (2022).
77. W. Wang, C. Yang, L. Bai, M. Li, and W. Li, *Nanomaterials*, **8**, 74 (2018).
78. G. Copetti, E. H. Nunes, T. O. Feijo, E. R. F. Gerling, E. Pitthan, G. V. Soares, M. Segala, and C. Radtke, *J. Mater. Chem. C*, **7**, 14672 (2019).
79. L. Yuan, T. Wang, T. Zhu, M. Zhou, and L. Huang, *J. Phys. Chem. Lett.*, **8**, 3371 (2017).
80. J. J. Snellenburg, S. P. Laptenok, R. Seger, K. M. Mullen, and I. H. M. van Stokkum, *J. Stat. Softw.*, **49**, 1 (2012).
81. T. Kato and T. Kaneko, *ACS Nano*, **10**, 9687 (2016).
82. B. Liu, C. Ma, D. Liu, and S. Yan, *ChemElectroChem.*, **8**, 3030 (2021).